Superior Efficiency Under PWM Harmonic Current in an Axial-Flux PM Machine for HEV/EV Traction: Comparison With a Radial-Flux PM Machine

Ren Tsunata, Masatsugu Takemoto, Jun Imai, Tatsuya Saito, and Tomoyuki Ueno

***Abstract*—This paper evaluates the harmonic current caused by a pulse width modulation (PWM) inverter and how it affects the efficiency of a novel axial-flux permanent-magnet machine using a ferrite permanent magnet (AF-FePM) in traction applications. First, differences between the finite element analysis (FEA) and experimental results are discussed using a prototype of the proposed AF-FePM. Second, the AF-FePM is compared with a commercially available radial-flux permanent-magnet machine using a Nd-sintered magnet (RF-NdPM). For both machines, the efficiency and loss are calculated using FEA when applying the sinusoidal and harmonic currents. Additionally, we present the superior efficiency of the AF-FePM under the PWM harmonic current during a WLTC driving cycle because the designed model employs the ferrite magnet and a round copper wire, unlike the RF-NdPM. Finally, motor and inverter losses at different switching frequencies are also evaluated. This paper eventually shows that the proposed AF-FePM would be one of the suitable candidates to enhance high efficiency under PWM harmonic current condition based on comprehensive discussion.**

***Index Terms*—Axial gap motor, axial-flux machine, carbon-fiber-reinforced plastic, ferrite magnet, iron loss, PWM drive, PWM harmonic current, radial-flux machine, soft magnetic composite, switching frequency, WLTC drive.**

I. Introduction

PERMANENT magnet synchronous machines (PMSMs) for traction applications need to be manufactured at low cost due to the increasing production volume of electric vehicles in recent years [1], [2]. We have proposed an axial-flux permanent magnet machine (AFPM) that achieves low cost by employing a ferrite permanent magnet (ferrite PM) and round copper wire, as shown in Fig. 1 [3]. Our proposed AFPM is referred to as AF-FePM in this paper. The AF-FePM can be manufactured at lower cost than a commercially available radial-flux permanent magnet machine (RFPM) with a neodymium-sintered PM (Nd-sintered PM) and rectangular copper wire (Fig. 2) [4]. The commercially available RFPM is mounted in a Honda Freed and is set as the target machine, which is referred to as RF-Nd-PM in this paper [5]. The high-performance RF-NdPM was chosen for the reference machine in this paper because it uses the same

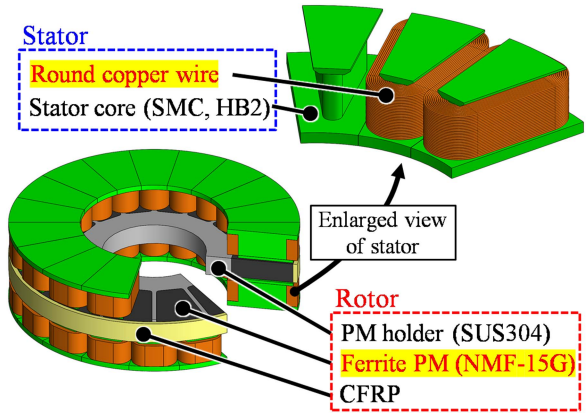

Fig. 1. 3D model of the proposed AF-FePM for traction applications.

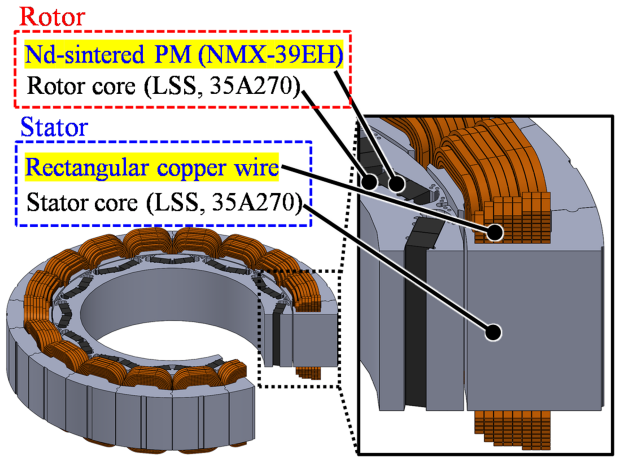

Fig. 2. 3D model of a commercially available RF-NdPM mounted in Honda Freed (target machine).

Manuscript received 7 February 2024; revised 12 April 2024 and 29 May 2024; accepted 31 May 2024. Date of publication 6 June 2024; date of current version 23 September 2024. This work was supported by the Japan Society for the Promotion of Science KAKENHI under Grant 24K17263. Paper 2024-EMC-0192.R2, presented at the 2023 IEEE Energy Conversion Congress and Exposition (ECCE), Nashville, TN, USA, Oct. 29–Nov. 02, and approved for publication in the IEEE Transactions on Industry Applications by the Electric Machines Committee of the IEEE Industry Applications Society [DOI: 10.1109/ECCE53617.2023.10362347]. *(Corresponding author: Ren Tsunata.)*

Ren Tsunata, Masatsugu Takemoto, and Jun Imai are with the Division of Industrial Innovation Sciences Graduate School of Natural Science and Technology, Okayama University, Okayama 700-8530, Japan (e-mail: tsunata@okayama-u.ac.jp; mtakemoto@okayama-u.ac.jp; imaij@okayama-u.ac.jp).

Tatsuya Saito and Tomoyuki Ueno are with the Sumitomo Electric Industries Ltd., Osaka 554-0024, Japan (e-mail: saitoutatsuya@sei.co.jp; uenotomoyuki@sei.co.jp).

Color versions of one or more figures in this article are available at https://doi.org/10.1109/TIA.2024.3410241.

Digital Object Identifier 10.1109/TIA.2024.3410241

TABLE I
TARGET SPECIFICATIONS OF THE AF-FEPM AND RF-NDPM

Parameters	Value	
	AF-FePM	RF-NdPM
Number of pole / slot	16p / 18s	12p / 18s
Winding type	Round wire	Rectangular wire
Permanent magnet	Ferrite PM	Nd-sintered PM
Max. power	22 kW	
Max. torque	160 Nm	
Max. speed	6800 rpm	
Max. inverter current	220 Arms	
DC bus voltage	173 V	
Total axial length	78.6 mm	
Outer diameter	261.6 mm	

concentrated winding stator as the proposed AF-FePM, making it easy to compare.

In [3], we proposed a novel rotor structure and suitable shapes for the tooth-tips of the AF-FePM. Additionally, we demonstrated that the proposed structure can compensate for the low remanence of the ferrite PM and the low magnetomotive force of the round copper wire. As a result, although the AF-FePM uses a ferrite PM and round copper wire, it is capable of achieving the required performance of the target RF-NdPM shown in Table I. On the other hand, comparison of the two machines in our previous research considered only analysis with a sinusoidal input current [3], but the input current during actual operation includes harmonic components caused by a PWM inverter [6].

The PWM harmonic current causes harmonic loss in each part in the proposed AF-FePM and target RF-NdPM, respectively. The effect of the PWM harmonic current on the RF-NdPM is large because of its Nd-sintered PM, rectangular copper wire, and laminated steel sheet (LSS). In contrast, we expect that the AF-FePM will suppress the increase in the PWM harmonic loss because of its ferrite PM, round copper wire, and soft magnetic composite (SMC). It is important, and would be useful, to understand differences in how the PWM harmonic current affects the efficiencies of AF-FePM and RF-NdPM over a wide operating region, but this has not been investigated yet.

Many research groups have investigated the influence of the PWM harmonic current on the losses in RFPMs [7], [8], [9]. However, there have been few reports on the influence on losses in AFPMs because three-dimensional finite element analysis (3D-FEA) is generally needed. In some studies, AFPMs have been investigated using approximate 2D-FEA [10], [11]. Additionally, in those studies, comparison with RFPM has not been performed. Therefore, this paper has the following aims:

1) Verify the accuracy of the PWM harmonic current used for FEA through experiments.
2) Perform a comprehensive comparison of the AF-FePM and the target RF-NdPM using FEA.

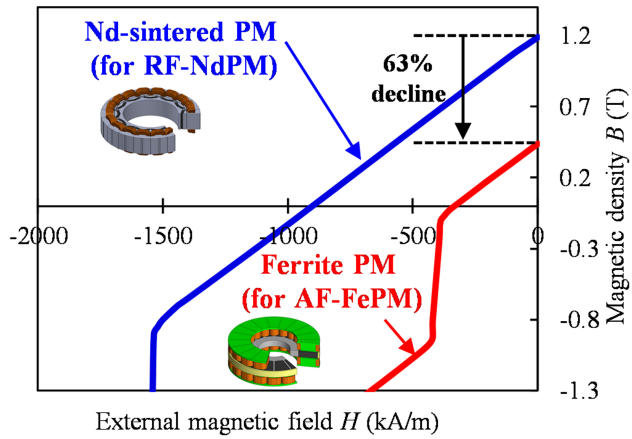

Fig. 3. *B-H* curves of Nd-sintered PM and ferrite PM.

3) Clarify the superiority of the proposed AF-FePM by considering the PWM harmonic loss in a WLTC driving cycle.
4) Evaluate total loss including inverter loss at different switching frequencies.

Only FEA results were reported in a previous conference paper at ECCE2023 [12]. The present paper includes newly added experimental results and additional FEA results. Furthermore, this paper newly includes the evaluation of the effects of the switching frequency on loss in both machines and inverters.

This paper is organized as follows. Section II describes the structures, features, and materials of the proposed AF-FePM and the target RF-NdPM. Additionally, the simulation results of the PWM harmonic current caused by the PWM inverters in both machines are also shown. Section III verifies the accuracy of the PWM harmonic current used for FEA through experiments. In Section IV, FEA is used to compare the efficiencies and losses of both machines when sinusoidal and PWM harmonic currents are applied. Section V presents a comparison of the total energy loss of both machines in a WLCT driving cycle, and demonstrates the superior efficiency of the AF-FePM compared with the RF-NdPM. Section VI evaluates the effect of switching frequency on motor and inverter losses, and discusses the appropriate switching frequency at frequently used operating area.

II. STRUCTURE OF THE TWO MACHINES AND ANALYSIS OF PWM HARMONIC CURRENTS

A. Materials and Structure

Figs. 1 and 2 show the structures and materials of the AF-FePM and the RF-NdPM. Table I lists the specifications of the AF-FePM and the RF-NdPM. The RF-NdPM is mounted on a commercially available hybrid vehicle (Honda Freed). In this paper, the proposed AF-FePM is compared with the RF-NdPM. Both machines have the same volume. Moreover, the axial length and outer diameter of both machines are 78.6 mm and 261.6 mm, respectively. The combination of poles and slots differ between them, however. The RF-NdPM uses 12 poles and 18 slots, while the AF-FePM uses 16 poles and 18 slots because the mechanical strength of a disk-shaped rotor can be improved. Additionally,

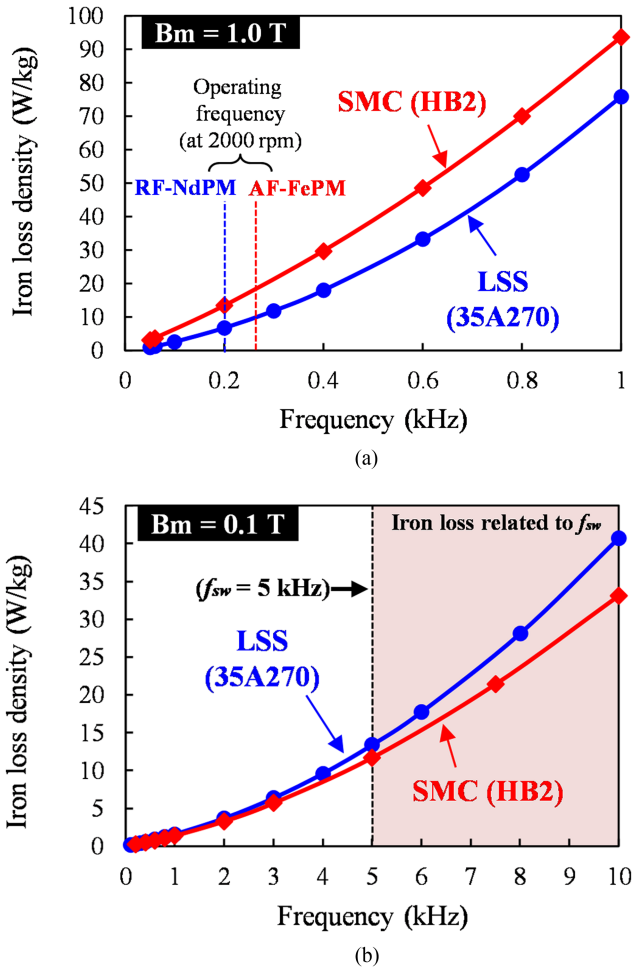

Fig. 4. Iron loss density of SMC (HB2, Sumitomo Electric Ind., Ltd.) and LSS (35A270).

the AF-FePM enables back-FEM with a low THD, owing to the 16 poles/18 slots combination [13].

The AF-FePM uses a ferrite PM, which helps reduce the cost of the permanent magnet. Fig. 3 shows the *B-H* properties of the Nd-sintered PM (NMX-39EH, Hitachi Metals, Ltd.) and the ferrite PM (NMF-15G, Hitachi Metals, Ltd.). The ferrite PM has a 63% lower residual magnetic flux density compared with the Nd-sintered PM. However, there is no PWM harmonic loss, including the eddy current loss in the ferrite PM, because of its near zero electric conductivity [14].

Furthermore, the AF-FePM uses a round copper wire, which can reduce the eddy current loss in the winding [4]. It can, therefore, be expected that the harmonic loss due to a PWM inverter is suppressed by the round copper wire. Moreover, Fig. 4 shows the iron loss properties of an SMC and an LSS (35A270), which were used for the magnetic cores in both machines. The SMC (HB2, Sumitomo Electric Industries, Ltd.) chosen for the AF-FePM has good iron loss properties compared with many SMC materials [15]. At low frequencies near the operating frequency, as shown in Fig. 4(a), the iron loss of the LSS is lower than that of the SMC. Additionally, the operating frequencies of the AF-FePM and the RF-NdPM differ at the same rotational speed due to the difference in the number of poles. Fig. 4(b) shows the iron loss in the high-frequency region. Unlike the low-frequency region, the SMC has lower iron loss than the LSS. Accordingly, this implies that the PMW harmonic iron loss due to an inverter in the SMC is lower than that in an LSS. Additionally, in [16], the harmonic iron loss of SMC (HB2) and LSS considering the DC-bias is compared. According to measured results, SMC can significantly suppress the increase in iron loss due to DC-bias, compared to LSS. In summary, the AF-FePM is likely to minimize the decrease in efficiency caused by the PWM harmonic loss. On the other hand, this means that if Nd-sintered PM or LSS is applied to AFPM, the advantage against the PWM harmonic current is likely to be lost.

B. PWM Harmonic Current Simulation

In this paper, the PWM harmonic current was calculated by a circuit simulator (PSIM, ver. 11.1.7). Fig. 5 shows schematic PSIM circuit and current control used to calculate the PWM harmonic current. The three-phase inverter is driven by the current control using typical feedback, as shown in Fig. 5(b). In this paper, co-simulation that combines current analysis with FEA was not performed in PSIM. The reason is that when co-simulation is performed, it is necessary to perform FEM at the same time as current analysis, and it takes a long time for the current to reach a steady state [17], [18]. Therefore, in this research, we input the harmonic current waveform analyzed with PSIM into the FEA software to finish the FEA with one period of electrical angle. As a result, analysis time can be reduced. On the other hand, when analyzing the harmonic current with PSIM, it is necessary to consider differences in spatial harmonics between the AF-FePM and RF-NdPM in order to perform accurate analysis. Therefore, we have adopted a "behavioral model" for the PMSM model used in PSIM. The behavioral model is an analysis model that has lookup tables for PMSM spatial harmonics, inductance [19]. The PWM harmonic currents of the AF-FePM and RF-NdPM were calculated in all operating areas under these prerequisites. In this section, the switching frequency was set to 5 kHz. The evaluation and clarification of the appropriate switching frequency for both machines including the inverter is detailed in Section VI.

Fig. 6 shows the simulation results of PWM harmonic currents in the two machines at 2000 rpm and 33 Nm. The area around this operating point is frequently used during the WLTC driving cycle. The analyzed PWM harmonic current of the AF-FePM has a higher operating frequency than the RF-NdPM because of the greater number of poles. As a result, the THD of the analyzed PWM harmonic current in the AF-FePM is also higher than that of the RF-NdPM, as shown in Fig. 6(a) and (b). The greater number of poles reduces the number of switching times per an electrical angle of 360 deg. Fig. 6(c) and (d) show that the harmonic components corresponding of the switching frequency of the AF-FePM are larger than those of the RF-NdPM. Accordingly, in terms of the input current, the AF-FePM is more susceptible to the target RF-NdPM.

III. Experimental Verification of PWM Harmonic Current Used for FEA

In this section, as a preliminary step toward the analytical comparison, we describe use of a prototype AF-FePM to confirm

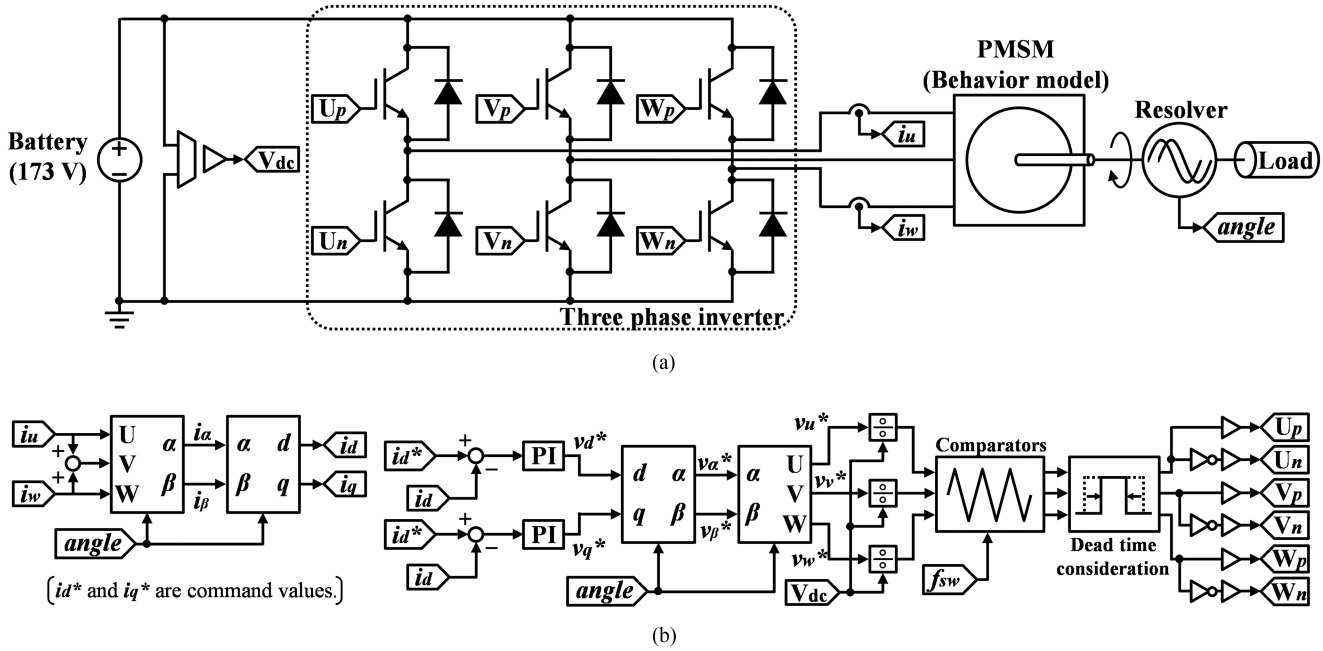

Fig. 5. Schematic PSIM circuit and current control for analyzing the PWM harmonic current waveforms of the AF-FePM and RF-NdPM. (a) Circuit configuration. (b) Control scheme.

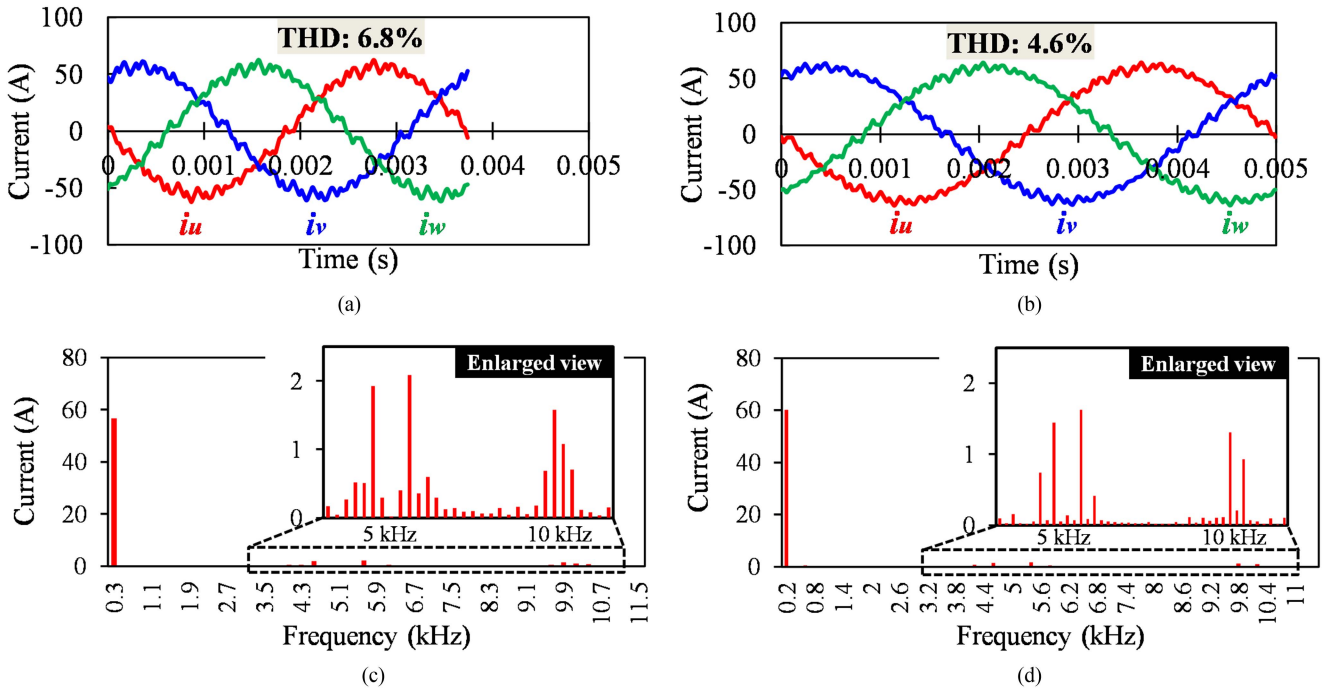

Fig. 6. Analyzed PWM harmonic current waveforms and spectra with switching ripple at 2000 rpm, 33 Nm, and $f_{sw} = 5$ kHz. (a) Current waveform of the AF-FePM (16 poles). (b) Current waveform of the RF-NdPM (12 poles). (c) Harmonic spectrum of the AF-FePM. (d) Harmonic spectrum of the RF-NdPM.

the accuracy of the PWM harmonic current used in FEA and its efficiency.

A. Prototype and Test Platforms

Fig. 7 shows the prototype of the AF-FePM. Fig. 7(a) and (b) show the rotor and stator, respectively. The AF-FePM uses a 16 pole/18 slot combination. In the rotor, the CFRP is directly wound around the ferrite PMs to increase the effective area of the magnet and enhance the mechanical strength simultaneously [3]. In the stator, the SMC and the round copper wire are used for the stator core and the winding, respectively. The tooth-tips of the stator core were inserted to the teeth. The entire stator was then molded with epoxy for cooling. We confirmed that the prototype can be manufactured and assembled without any issues. In this case, the tooth-tip and the tooth need to be separated. On the other hand, this shape can be

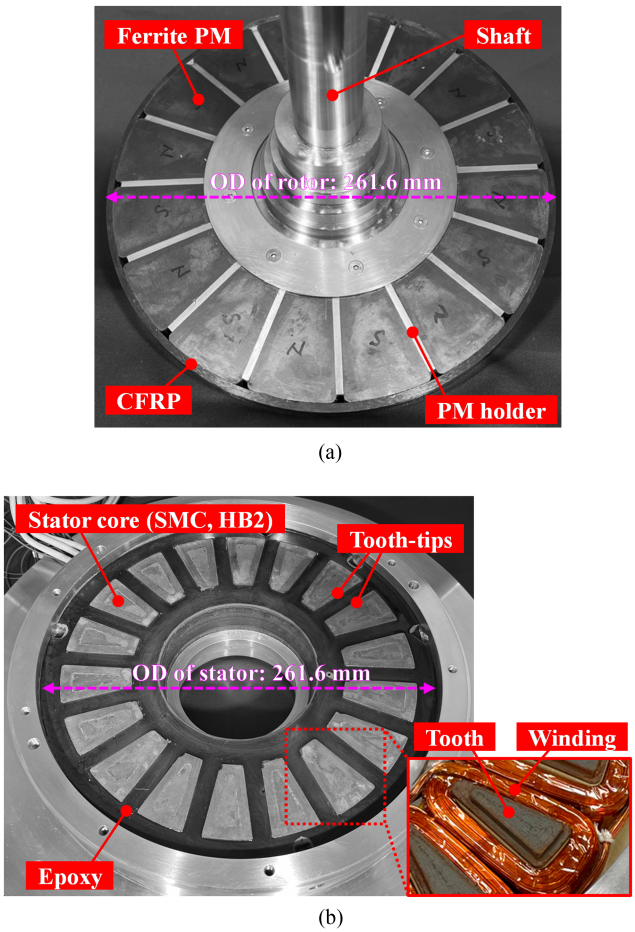

Fig. 7. Prototype of the proposed AF-FePM. (a) Rotor (16 poles). (b) Stator (18 slots).

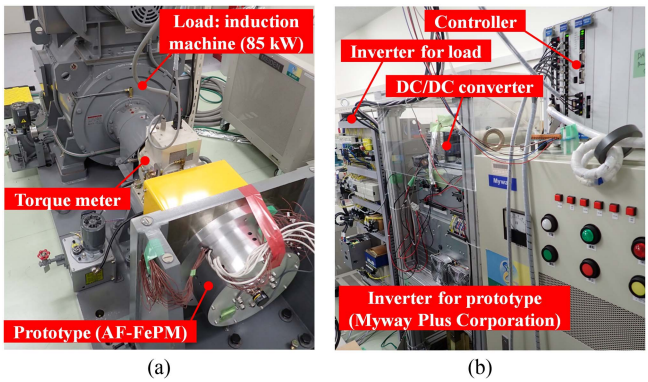

Fig. 8. Test platform and drive system. (a) Prototype and load. (b) Controller and inverters.

manufactured by one pressing process in mass production, as proposed in [20]. Additionally, the AF-FePM has a double-stator and single-rotor structure [21]. Hence, the prototype has the two stators.

Fig. 8 shows the test platform and drive system used in this paper. The prototype of the AF-FePM is connected to an induction machine as a load via a torque meter. A three-phase inverter (Myway Plus Corporation) was used to drive the prototype.

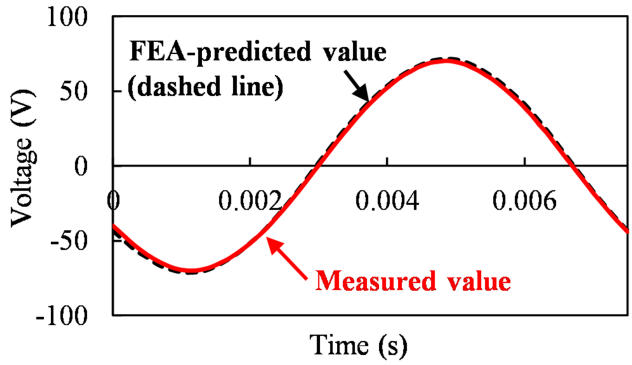

Fig. 9. Comparison of FEA-predicted and measured back-EMF (1000 rpm).

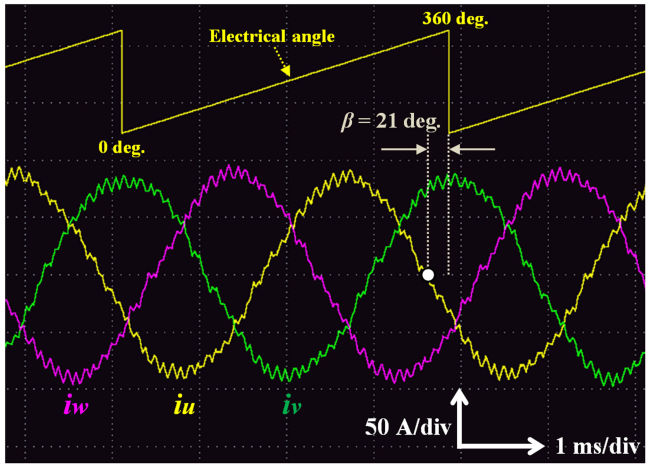

Fig. 10. Screenshot of an oscilloscope measuring the input PWM harmonic current waveforms and electrical angle at 2000 rpm, 60 Arms, and $\beta = 21$ deg.

B. Experimental Results

Fig. 9 shows the FEA-predicted and measured no-load back-EMF of the AF-FePM at 1000 rpm. The error of the voltage effective value between the two waveforms is 0.5%, indicating that the prototype was manufactured with high accuracy. Fig. 10 shows a screenshot of an oscilloscope (DL950, Yokogawa Test & Measurement Corporation) measuring PWM harmonic currents at the operating point that has the highest efficiency in the AF-FePM. The rotational speed, current effective value, and current phase angle β were 2000 rpm, 60 Arms, and 21 deg., respectively. Furthermore, the switching frequency f_{sw} of the inverter for the prototype was set to 5 kHz. From the phase relationship with the electrical angle, we can see that the current phase angle β can be controlled as expected.

Fig. 11 shows a comparison of the calculated and measured PWM harmonic currents ($f_{sw} = 5$ kHz). The calculated and measured PWM harmonic current waveforms agree well, and Fig. 11(b) shows the spectra of both. The total harmonic distortions (THD) of the calculated and measured currents are 4.79% and 4.87%, respectively. There is a slight error in the amplitude of the component corresponding to the switching frequency. The slight error might be caused by some control factor and parasitic components. Such a phenomenon has also been reported elsewhere [9], [22], [23]. However, in this result,

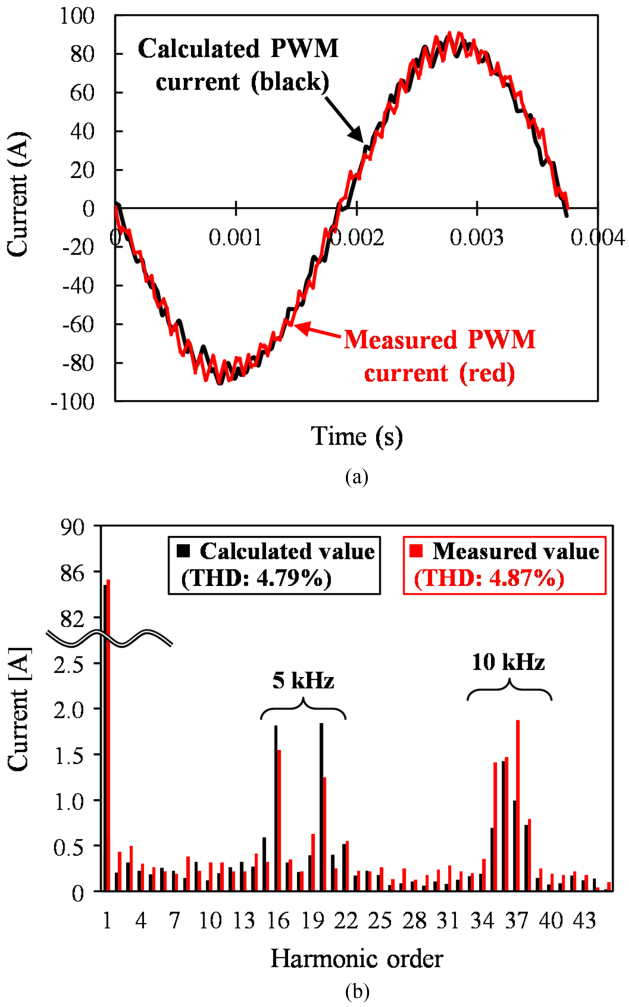

Fig. 11. Comparison of calculated and measured PWM harmonic currents when the switching frequency is 5 kHz. (a) Current waveforms. (b) Spectrum.

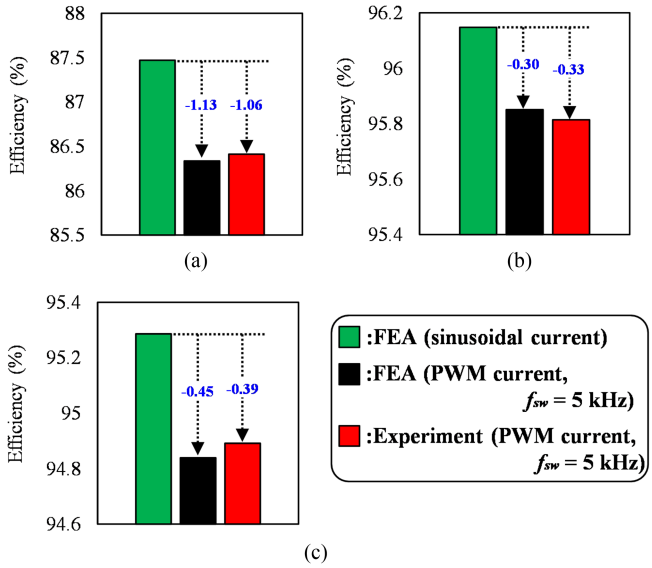

Fig. 12. Comparisons of FEA-predicted and measured efficiency. (a) Low-speed and low-torque point (1313 rpm (base speed), 5 Nm, 10 Arms). (b) The highest efficiency point (2000 rpm, 50 Nm, 60 Arms). (c) High-speed point (4000 rpm, 20 Nm, 20 Arms).

the accuracy of the calculated PWM harmonic current is very high, which indicates that the influence of the PMW harmonic current on the losses can be predicted by the FEA.

In general, total loss in the experiment is larger compared with the FEA result due to the mechanical loss and the increase in iron loss. Iron loss is increased by the PWM harmonic current. The mechanical loss can be calculated by subtracting the total loss in the FEA from the total loss in the experiment under no-load condition. By subtracting this from the experimental results, it is possible to calculate efficiency by considering only the increase in loss in the PWM harmonic current.

Fig. 12 shows comparisons of the FEA-predicted and measured efficiencies at three representative operating points. The two FEA-predicted efficiencies are calculated when applying sinusoidal and PWM (f_{sw} = 5 kHz) harmonic currents. The measured total loss was obtained with a power meter (WT1800, Yokogawa Test & Measurement Corporation). Then, the efficiency in the experiment was calculated by subtracting the mechanical loss from the total loss. Fig. 12(a) shows the efficiencies at a low-speed and low-torque operating point. At this operating point, the total loss is small because the output power is low. This means that the influence of the PWM harmonic loss on the efficiency tends to be high. Therefore, the FEA-predicted value when applying the PWM current is much lower than with the sinusoidal current. As a result, the FEA-predicted value with the PWM current is very close to the measured efficiency. Fig. 12(b) and (c) show the efficiencies at the highest efficiency point and the high-speed operating point, respectively. Similarly, the FEA-predicted efficiencies with the PWM harmonic currents at these operating points also show values that are very close to the efficiency obtained in experiments. From these results, we conclude that the efficiency of actual machines can be predicted with relatively high accuracy by considering PWM harmonic currents in FEA.

IV. Loss and Efficiency Calculation Using FEA

A. Each Loss At A Frequently Used Operating Point

In this research electromagnetic properties and losses were calculated with FEA using JMAG Designer (version 21.0). The harmonic iron loss calculated by FEA using JMAG Designer does not consider the DC-bias. In this paper, the proposed AF-FePM and the target RF-NdPM were analyzed using 3D-FEA and 2D-FEA, respectively. Fig. 13 and Table II show mesh models of the two machines and winding parameters, respectively. In the two machines, a very fine mesh was set, in order to accurately analyze the eddy current in the winding. In particular, the analysis time is extremely long because the AF-FePM is evaluated by 3D-FEA. The coil fill factor C_f of the proposed AF-FePM is lower than that of the RF-NdPM because the round copper wire is used, as shown in Table II.

When predicting the eddy current loss of a magnet using 2D-FEA, the error from 3D-FEA may become large. This is due to the inability to accurately simulate the eddy current path with 2D-FEA, and the error increases as the axial length of the model becomes smaller [24]. Furthermore, it is difficult to predict the eddy current loss using 2D-FEA when the PM is divided in the

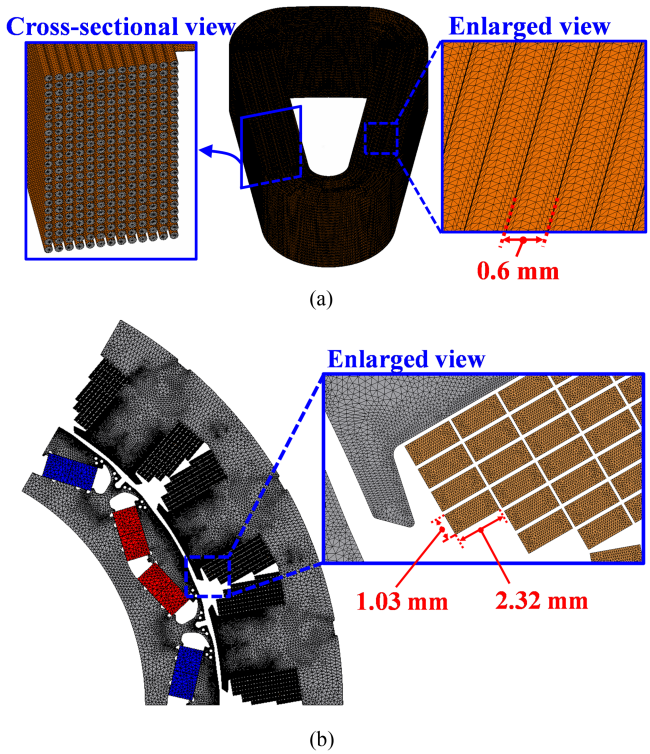

Fig. 13. Mesh models of two machines for FEA. (a) AF-FePM. (b) Target RF-NdPM.

TABLE II
WINDING PARAMETERS OF THE AF-FEPM AND RF-NDPM

	AF-FePM	RF-NdPM
Winding type	Round	Rectangle
No. of parallels N_p	11	1
Wire diameter D_w [mm]	Φ0.6	-
Wire size [mm]	-	1.03×2.32
No. of turns N_t [turns]	34	55
Coil fill factor C_f [%]*	50	70

(*$C_f = [(D_w/2)^2 \pi N_t N_p]/S_w \times 100$ [%])

axial direction [25]. On the other hand, if the PM is not divided in the axial direction, the error in the eddy current loss of the PM obtained by 2D-FEA and 3D-FEA is small [26], [27], [28]. In the target RF-NdPM the Nd-sintered PMs are not divided in the axial direction, and, hence, it is possible to accurately calculate loss, even with 2D-FEA.

Fig. 14 shows the magnetic flux density in the stator core of the AF-FePM at 2000 rpm and 33 Nm. The armature current is low at this operating point. Accordingly, magnetic saturation does not occur in the stator core. Fig. 15 shows the torque waveforms of the AF-FePM at the corresponding operating point when a sinusoidal current and PWM harmonic current with $f_{sw} = 5$ kHz are applied. The average torque of the AF-FePM is 33 Nm regardless of input currents. However, torque ripple of the AF-FePM increases when the harmonic current is applied because

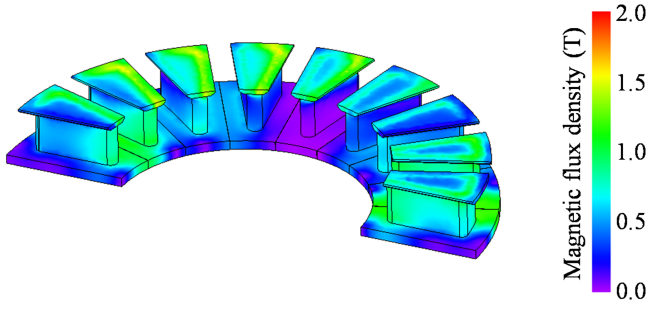

Fig. 14. Magnetic flux density distributions of the AF-FePM when applying a PWM harmonic current with $f_{sw} = 5$ kHz (2000 rpm, 33 Nm).

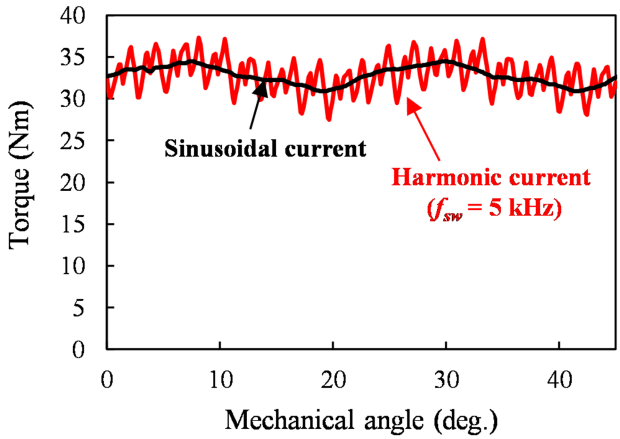

Fig. 15. Torque waveform of the AF-FePM analyzed with sinusoidal and harmonic currents (2000 rpm, 33 Nm, $f_{sw} = 5$ kHz).

of slight changes in the magnetic flux during operation. This change in magnetic flux causes additional harmonic iron loss [29], [30].

Fig. 16 shows the iron loss density distribution in the SMC stator core of the AF-FePM at 2000 rpm and 33 Nm. Fig. 16(a) and (b) show the distribution at a corresponding operating frequency of 266 Hz when sinusoidal and PWM harmonic currents are applied, respectively. The fundamental amplitude of sinusoidal and harmonic currents is the same, and, therefore, the iron loss density distributions are almost the same. Regions indicating high magnetic flux density in Fig. 14 have high iron loss density. Fig. 16(c) and (d) show the iron loss density distributions at 5.6 kHz corresponding to the PWM harmonic components. In Fig. 16(c) the overall iron loss density is zero because a sinusoidal current is applied. In contrast, the iron loss density in Fig. 16(d) is obviously higher than in Fig. 16(c). This implies that the PWM harmonic iron loss corresponding to the switching frequency occurs in the stator core.

Fig. 17 shows a comparison of the iron loss spectra in the stator cores of the tow machines at 2000 rpm and 33 Nm when sinusoidal and PWM harmonic currents are applied, respectively. Both analyses with sinusoidal and PWM harmonic currents were performed with the same analysis resolution. Fig. 17(a) shows a comparison of the iron loss in the AF-FePM. The low-order harmonic iron losses in the two cases are almost the same regardless of the input currents. However, if the PWM harmonic current is applied, the high-order harmonic iron loss

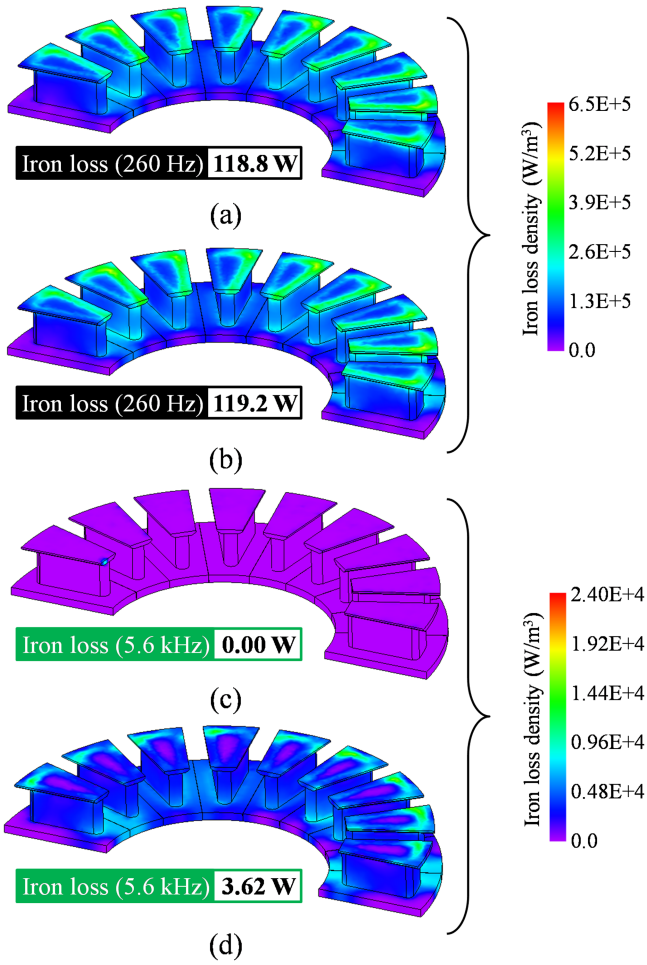

Fig. 16. Iron loss density distributions in the stator core of the AF-FePM (2000 rpm, 33 Nm). (a) Fundamental iron loss at (266 Hz, sinusoidal current). (b) Fundamental iron loss (266 Hz, harmonic current). (c) Harmonic iron loss (5.6 kHz, sinusoidal current). (d) Harmonic iron loss (5.6 kHz, harmonic current).

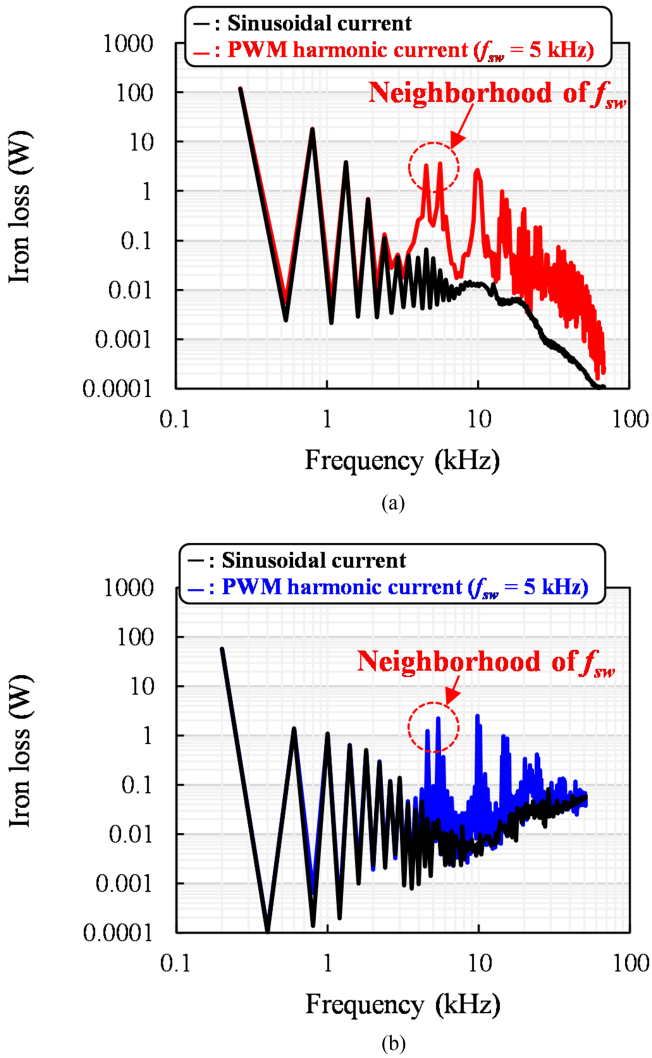

Fig. 17. Comparison of the spectrum of iron loss in the stator cores when applying sinusoidal and PWM harmonic currents (2000 rpm, 33 Nm). (a) The AF-FePM. (b) The RF-NdPM.

occurs. As a result, it can be seen that the stator core iron loss increases for frequencies over 5 kHz, which is the switching frequency. Additionally, the higher the frequency becomes, the smaller the iron loss that occurs, regardless of the input current. This is because the iron loss of the SMC is small in the high-frequency region, as shown in Fig. 4(b). Fig. 17(b) shows a comparison of the stator iron loss in the LSS of the RF-NdPM. The low-order harmonic iron losses in the two cases are almost the same regardless of the input currents, which is a similar trend to what was seen in the AF-FePM. On the other hand, the higher the frequency, the larger the high-order harmonic iron loss. This is because the LSS tends to have a larger iron loss at high-frequency regions compared to the SMC, as shown in Fig. 4. Furthermore, if the PWM harmonic current is applied, then high-order harmonic iron loss occurs.

Table III lists the iron loss in the stator cores of the two machines at 2000 rpm and 33 Nm. Under sinusoidal current conditions, the iron loss of the AF-FePM is larger than that of the RF-NdPM due to the large low-order iron loss of the SMC. Moreover, the iron loss of both machines is increased in cases

TABLE III
SUMMARY OF STATOR IRON LOSS AT 2000 RPM AND 33 NM

	AF-FePM	RF-NdPM
Sinusoidal current	138.8 W	63.6 W
PWM Harmonic current (f_{sw} = 5 kHz)	162.0 W	90.3 W
Rate of increase	16.7%	42.0%

where PWM harmonic currents are considered. However, the rate of increase in the iron loss of the AF-FePM is much lower than that of the RF-NdPM. This is because the iron loss density of the SMC in the high-frequency region is lower than the LSS, as shown in Fig. 4.

Fig. 18 shows the efficiency and losses of the two machines when applying the sinusoidal and analyzed PWM harmonic currents at 2000 rpm and 33 Nm. The total loss calculated for

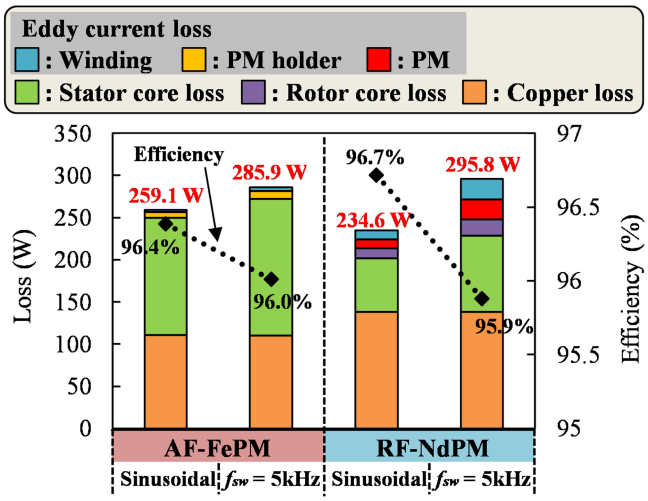

Fig. 18. Loss and efficiency when applying a sinusoidal current and the analyzed PWM harmonic current with $f_{sw} = 5$ kHz (2000 rpm, 33 Nm).

the sinusoidal current in the AF-FePM is 9.5% larger than in the RF-NdPM because the iron loss of the SMC is large in the low-frequency region. In contrast, the total loss simulated by the PWM harmonic current with $f_{sw} = 5$ kHz in the AF-FePM is 3.3% smaller than that in the RF-NdPM. This means that the magnitude relation of the total loss and the efficiency in both machines is reversed by the PWM harmonic components in the input current. In the RF-NdPM the increasing ratio of the eddy current loss in the Nd-sintered PM and the rectangular copper wire is high. Additionally, the increasing ratio of the iron loss in the RF-NdPM is higher than in the AF-FePM because the iron loss of the SMC is smaller at $f_{sw} = 5$ kHz than in the LSS, as shown in Table III. Hence, the AF-FePM can moderate the increase in harmonic loss despite having a higher THD of input current.

B. Loss and Efficiency Over A Wide Operating Range

Fig. 19 shows the THD of the analyzed PWM harmonic current of the two machines at 2000 rpm. The THD of the AF-FePM is higher than that of the RF-NdPM in all areas because of the greater number of poles. In the region where the torque is small the THD of both machines is high because the fundamental amplitude of the armature current is small.

Fig. 20 shows a reduction in the efficiency under the PWM harmonic currents and the efficiency of the two machines at 2000 rpm. Although the THD of the PWM harmonic current in the AF-FePM is higher, the decrease in efficiency caused by the PWM harmonic current is lower than in the RF-NdPM (Fig. 20(a)). As a result, for the PWM harmonic current the torque at which the efficiency of both machines is reversed shifts to 22 Nm from 40 Nm (Fig. 20(b) and (c)), and the AF-FePM exhibits higher efficiency over a wider area. In the AF-FePM, the iron loss changes greatly

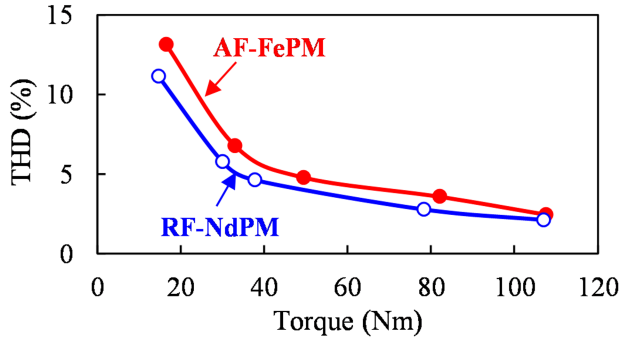

Fig. 19. THD of the analyzed PWM harmonic current at $f_{sw} = 5$ kHz (2000 rpm).

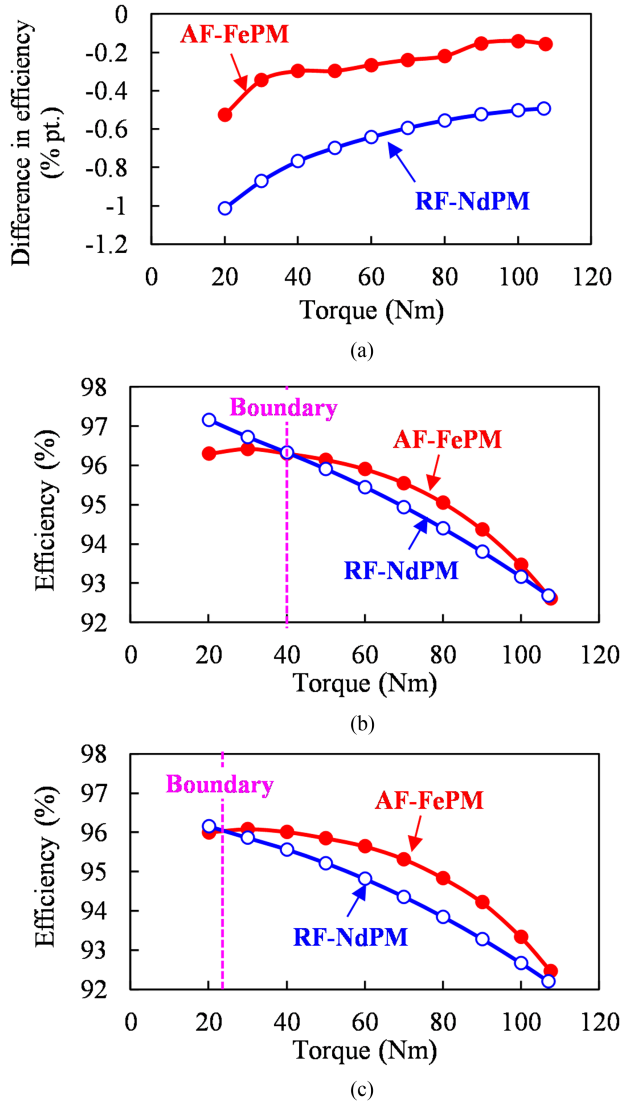

Fig. 20. Efficiency properties of the AF-FePM and RF-NdPM at 2000 rpm. (a) Reduction of efficiency due to the PWM harmonic current. (b) Efficiency calculated for the sinusoidal current. (c) Efficiency calculated for the analyzed PWM harmonic current at $f_{sw} = 5$ kHz.

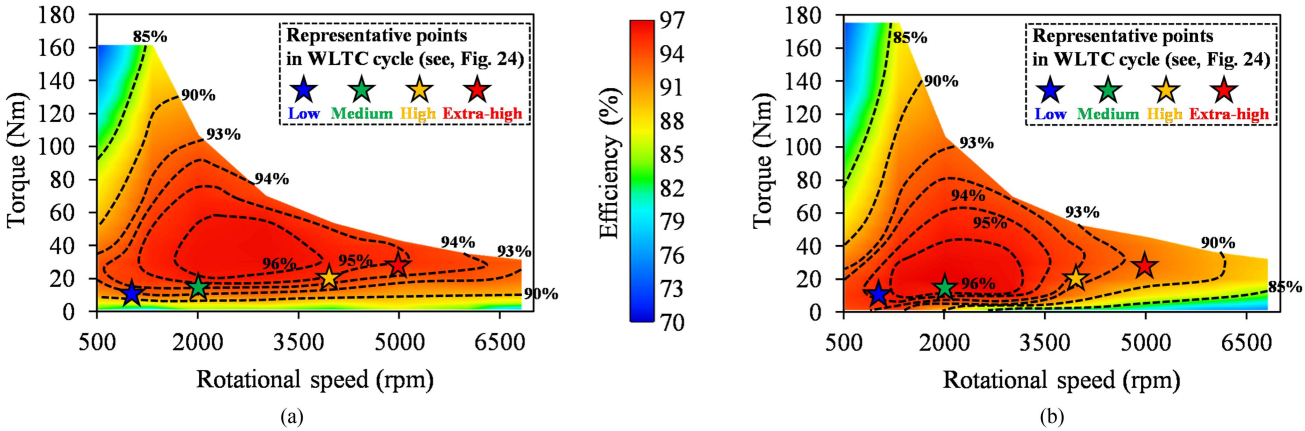

Fig. 21. Efficiency maps calculated under the sinusoidal current condition. (a) The proposed AF-FePM. (b) The target RF-NdPM.

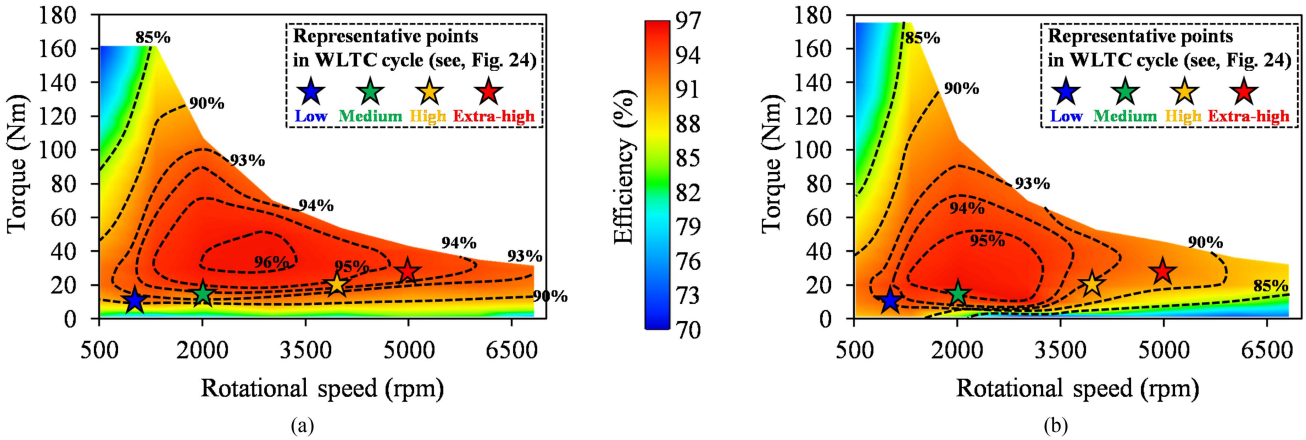

Fig. 22. Efficiency maps calculated under the PWM harmonic current condition with $f_{sw} = 5$ kHz. (a) The proposed AF-FePM. (b) The target RF-NdPM.

with respect to the magnetic flux density of the SMC used in the stator core. As a result, the efficiency of the AF-FePM changes secondarily.

Fig. 21 shows efficiency maps calculated from the sinusoidal currents in the two machines, each of which has a high-efficiency area of over 96%. In addition, the frequently used representative operating points of each phase in WLTC driving cycle are also plotted on the maps. The AF-FePM has much higher efficiency than the RF-NdPM in the high-speed region because its eddy current loss in the round copper wire and ferrite PM is extremely low. In contrast, as rotational speed increases, the efficiency of the RF-NdPM becomes markedly lower than that of the AF-FePM due to the eddy current loss in the Nd-sintered PM and the rectangular copper wire. Specifically, when both machines output 22 kW at the maximum rotational speed of 6800 rpm, the winding eddy current loss of the target RF-NdPM is 1.0 kW, while the proposed AF-FePM can suppress it to approximately 0.2 kW [31]. As shown by the representative operating points of high phase and extra-high phase, both machines also operate in the high-speed region in WLTC driving cycle, which is likely to affect the total energy loss. However, in the low-speed and low-torque region the efficiency of the RF-NdPM is higher than that of the AF-FePM because the LSS exhibits lower iron loss compared with the SMC.

Fig. 22 shows efficiency maps considering the PWM harmonic loss caused by PWM switching at $f_{sw} = 5$ kHz. As mentioned in the previous section, the AF-FePM can minimize the effects of the PWM harmonic current. Consequently, although the THD of the PWM harmonic current is high, the AF-FePM can maintain high efficiency over a wide operating area. In contrast, the region with efficiency of over 96% is not seen in the efficiency map of the RF-NdPM because of the large effect of the PWM harmonic current.

Fig. 23 presents maps of the reduction in efficiency (efficiency under the PWM harmonic current subtracted from that under the sinusoidal current). In the two machines the effect of the PWM harmonic loss on the efficiency is large in the low-torque region because the THD of the PWM harmonic current is high in these areas. However, the reduction in efficiency of the AF-FePM is much lower than that of the RF-NdPM. Accordingly, although the AF-FePM has both a greater number of poles and a harmonic current with higher THD than the RF-NdPM, it is possible to suppress the decrease in efficiency. As a result, the AF-FePM can

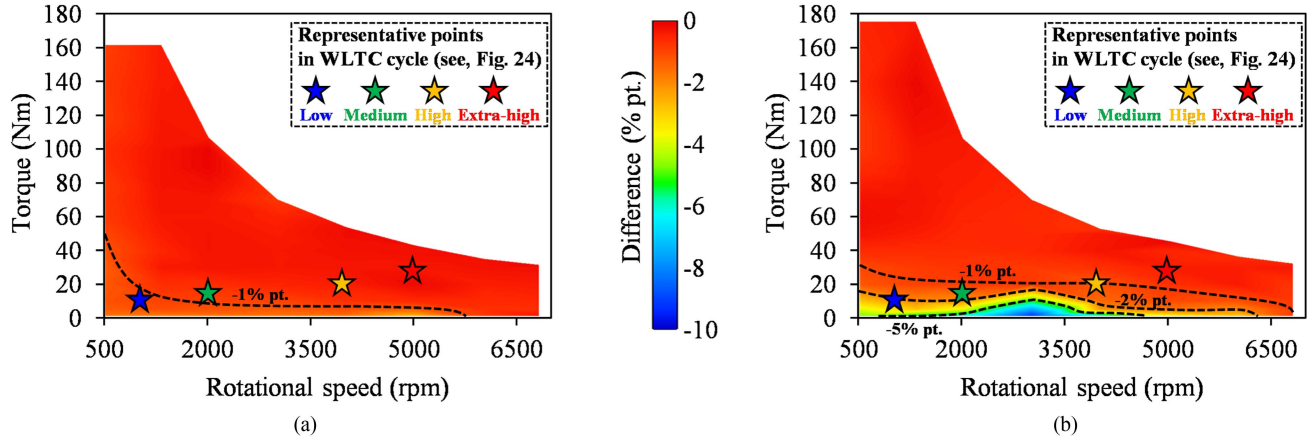

(a) (b)

Fig. 23. Maps of the reduction in efficiency, calculated by subtracting the efficiency with the PWM harmonic current from the efficiency with the sinusoidal current. (a) The proposed AF-FePM. (b) The target RF-NdPM.

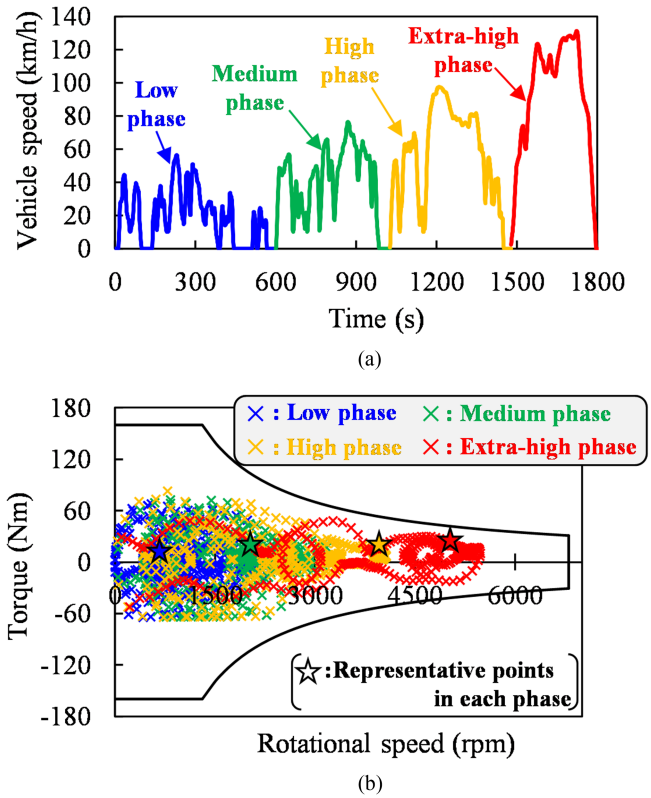

(a) (b)

Fig. 24. The vehicle driving cycle (WLTC class 3) and the corresponding operating points of the AF-FePM and RF-NdPM. (a) Vehicle speed pattern. (b) Corresponding operating points.

maintain high efficiency at the representative operating points in the WLTC driving cycle.

V. Comparison Based on a WLTC Driving Cycle

Fig. 24 shows a vehicle driving cycle (WLTC class 3) and the corresponding operating points of the two machines [32]. In this paper the characteristics of both machines are evaluated using these operating patterns. In addition, the frequently used representative operating points of each phase in WLTC driving cycle are also plotted. Fig. 25 shows the total loss in both machines during the WLTC driving cycle, which is calculated based on the map data shown in Figs. 21 and 22. Fig. 25(a) shows the total loss in both machines calculated using sinusoidal currents. In the low, medium, and high phase modes the AF-FePM has more moments with higher total loss compared to the RF-NdPM. One reason for this is that both machines frequently operate in the low-torque region where the RF-NdPM has higher efficiency in these three modes. On the other hand, in the extra-high phase mode both machines frequently operate in the high-speed region, as shown in Fig. 24(b). As a result, the total loss of the AF-FePM is noticeably smaller than that of the RF-NdPM, as shown in Fig. 25(a). In the high-speed and large-torque region the output power is large, and, therefore, the difference in efficiency tends to affect the total loss.

Fig. 25(b) indicates the same comparison between the two machines when the PWM harmonic current with $f_{sw} = 5$ kHz is applied. As mentioned previously, the AF-FePM can restrain the decrease in efficiency, especially in the low-torque area. Therefore, the AF-FePM can avoid increasing the total loss in the low, medium, and high phase modes. On the other hand, the RF-NdPM exhibits a larger decrease in efficiency when considering the PWM harmonic current, leading to a large total loss compared to the AF-FePM. Additionally, in the high and extra-high phase modes it can be observed that the total loss difference between the two machines has increased.

Fig. 26 shows the total energy loss of the two machines during the WLTC driving cycle. The values in Fig. 26 are obtained by integrating the graph in Fig. 25. The AF-FePM has a larger loss than the RF-NdPM in the low, medium, and high phase modes when considering the sinusoidal current because the efficiency of the RF-NdPM is higher in the low-speed and low-torque regions. However, the energy loss of the AF-FePM in the extra-high phase is 19.0% lower. Consequently, the total energy loss of both machines is almost the same when applying the sinusoidal current. On the other hand, in the case where the PWM harmonic current was considered the total energy loss of the RF-NdPM increased by 21.4%. In contrast, the AF-FePM can limit the increase in the total energy loss to 8.0%. As a result,

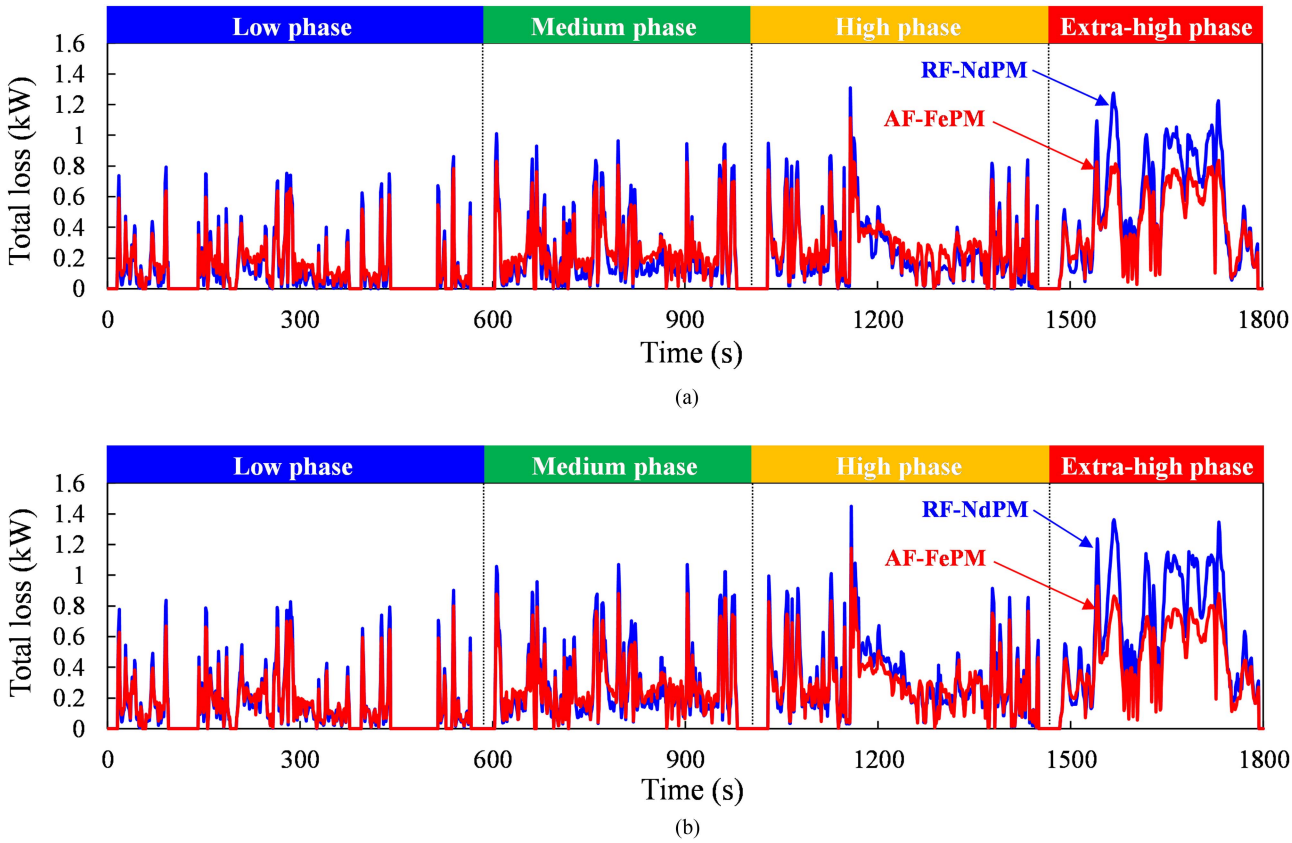

Fig. 25. Total loss in the AF-FePM and RF-NdPM during WLTC cycle. (a) Sinusoidal current operation. (b) PWM harmonic current operation ($f_{sw} = 5$ kHz).

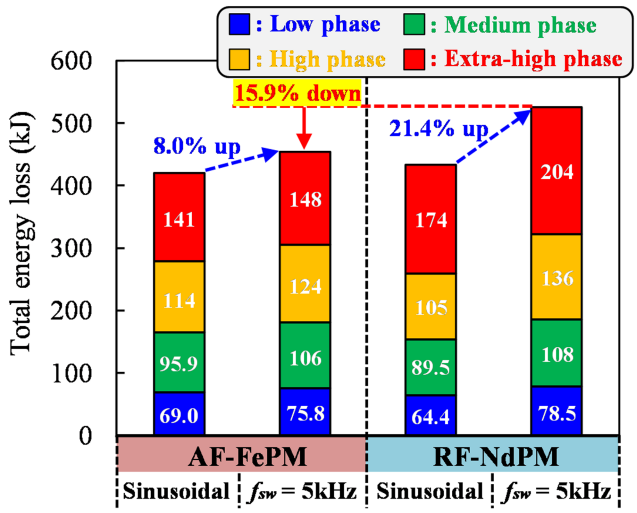

Fig. 26. Total loss of the AF-FePM and RF-NdPM during the WLTC driving cycle and a comparison based on the presence/absence of the PWM harmonic components in the input current.

the AF-FePM can achieve 15.9% lower total energy loss with the PWM harmonic current than the RF-NdPM.

Additionally, the total energy loss in the low, medium, and high phase modes of the AF-FePM is 5.2% smaller than that in the RF-NdPM. Hence, the relationship for the total energy loss between the two machines is reversed. Furthermore, in the AF-FePM the increase in total energy loss can be restrained when a low switching frequency is used, as in this investigation. This means that the AF-FePM can reduce inverter loss and improve system efficiency. In addition to having better thermal properties than RFPMs [33], the AF-FePM can suppress the rise in temperature because the total energy loss is small.

VI. Impact of Switching Frequency on Total Loss Considering Three Phase Inverter

In the previous sections, we showed that AF-FePM can suppress loss in harmonic currents. On the other hand, various techniques exist to reduce harmonic currents and corresponding losses. For example, harmonic currents can be suppressed by using a sine wave filter [34]. However, the system becomes larger and costs increase because additional components such as inductors are required. Furthermore, next-generation semiconductors such as SiC and GaN devices can suppress device switching loss even when the switching frequency is increased, making it possible to increase system efficiency [35]. Hori et al. [36] discusses variable switching frequency technology that uses GaN devices to increase the system efficiency considering motors and inverters. On the other hand, SiC and GaN devices also have the problem of increased costs and GaN's low withstand voltage. Additionally, [37] proposes a method of suppressing harmonic current by switching using carrier phase shift technique. In [38], the harmonic current is suppressed by optimizing the switching sequence. However, [37] and [38] require multi-inverters, which increases the size of the system.

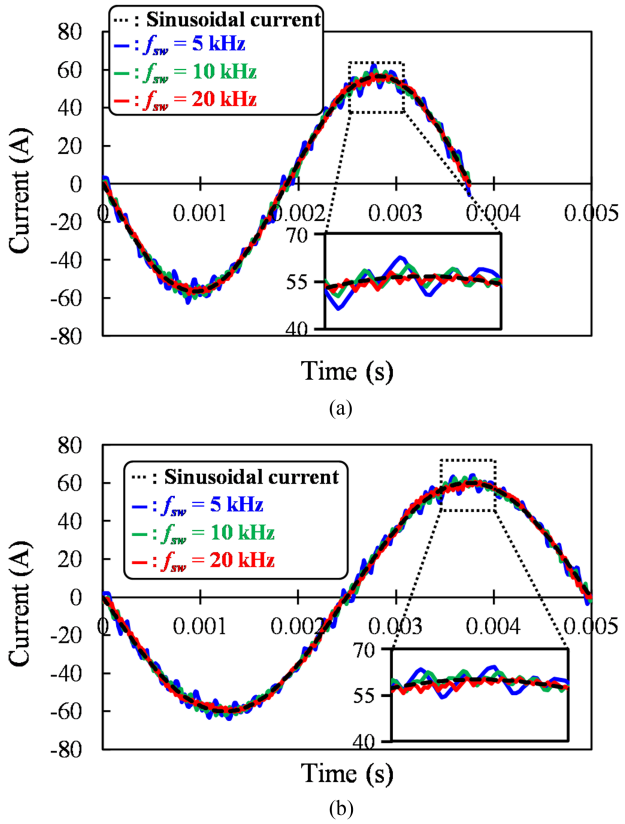

Fig. 27. Analyzed harmonic currents at different switching frequency at 2000 rpm and 33 Nm. (a) AF-FePM (40 Arms). (b) RF-FePM (42.5 Arms).

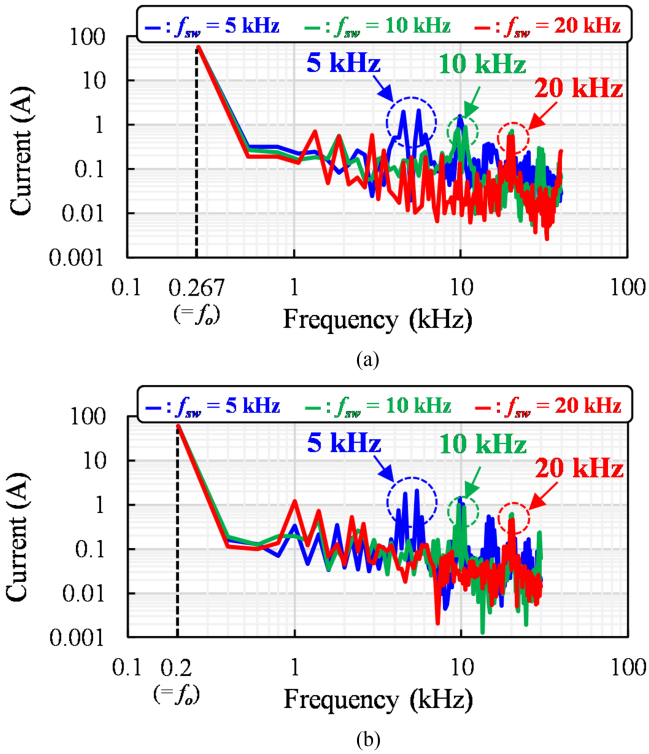

Fig. 28. The spectra of input harmonic current in both machines at 2000 rpm and 33 Nm. (a) AF-FePM (40 Arms). (b) RF-NdPM (42.5 Arms).

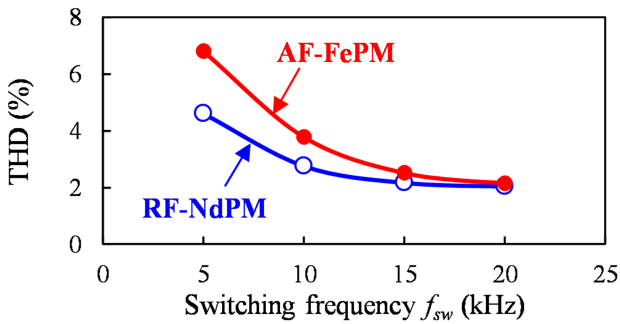

Fig. 29. Comparison of THD of the input harmonic currents for both machines at 2000 rpm and 33 Nm.

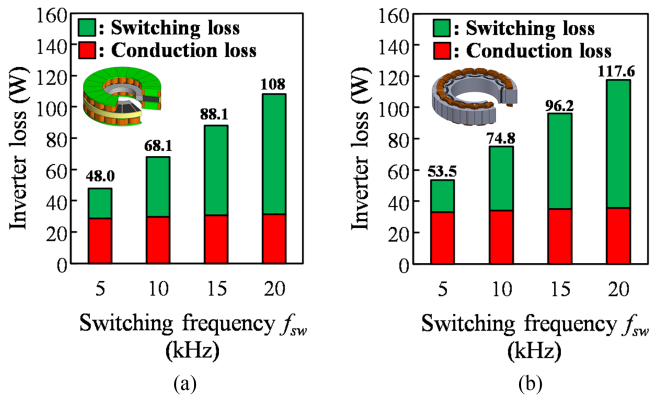

Fig. 30. Inverter losses used for the AF-FePM and RF-NdPM at different switching frequencies (2000 rpm and 33 Nm). (a) AF-FePM (40 Arms). (b) RF-NdPM (42.5 Arms).

From the above, countermeasures for the harmonic current generally have disadvantages such as increased costs and larger systems. On the other hand, the AF-FePM proposed in this paper can suppress an increase in loss even at low switching frequencies. Hence, it may be possible to improve system efficiency by lowering the switching frequency f_{sw} in inverters using regular Si devices. Therefore, this section discusses harmonic current waveforms and their THD, inverter loss, and total loss considering three-phase inverter as the switching frequency is changed.

Fig. 27 shows analyzed harmonic current waveforms of AF-FePM and RF-NdPM at different switching frequencies at frequently used operating points (2000 rpm, 33 Nm). Additionally, Fig. 28 indicates the spectra of the harmonic currents, showing peaks corresponding to each switching frequency. Furthermore, Fig. 29 shows the THD of the harmonic currents with respect to the switching frequency f_{sw} in both machines. When the switching frequency is increased for both machines, THD decreases, and at $f_{sw} = 20$ kHz, the waveform becomes close to a sine wave. As a result, the difference between both machines disappears. On the other hand, as shown in Section II, in the case of $f_{sw} =$ 5 kHz, the THD of the input current is higher for the proposed AF-FePM.

Fig. 30 shows the inverter losses for both machines at different switching frequencies. The considered inverter in this paper employs A 400 V Si-MOSFET as switching devices. Inverter losses are generally classified into switching loss and conduction

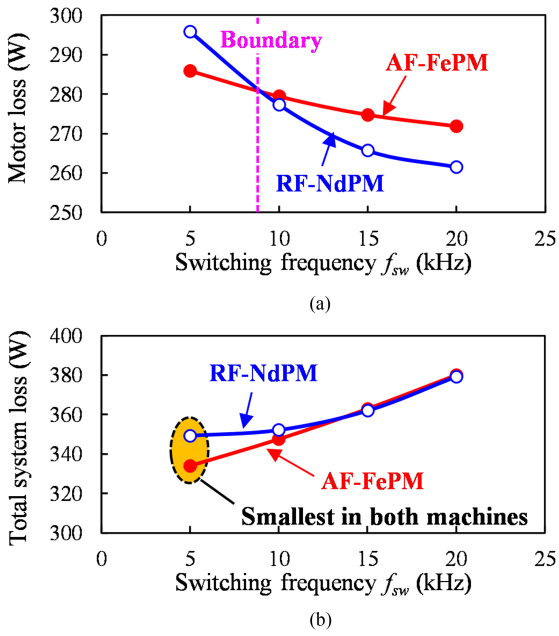

Fig. 31. Motor loss and total system loss including inverter loss of both machines versus switching frequency at 2000 rpm and 33 Arms. (a) Motor loss. (b) Total system loss.

loss, and can be predicted mathematically [39], [40]. In this paper, inverter losses in the system for AF-FePM and RF-NdPM were calculated based on [39]. As the switching frequency is increased, the switching loss linearly increases in the inverter of both machine systems. As a result, at this operating point, the switching loss become dominant at $f_{sw} = 20$ kHz. Furthermore, the conduction loss is hardly affected by the switching frequency. In addition, total inverter loss of RF-NdPM is slightly larger than that of the AF-FePM because the input current is larger.

Fig. 31 indicates the motor loss and the total loss including the inverter loss at different switching frequencies. As the switching frequency decreases, the loss increases for both machines, but the change is smaller for the AF-FePM. As a result, at high switching frequencies, the AF-FePM has larger loss than that of the RF-NdPM, but at $f_{sw} = 5$ kHz, AF-FePM can achieve lower loss. Furthermore, Fig. 31(b) shows the total loss including inverter loss, and it can be seen that in both cases, the lower the switching frequency, the smaller the total loss. Therefore, it is possible to reduce system loss by setting the switching frequency to $f_{sw} = 5$ kHz in this investigation.

In addition, in the high switching frequency range, the total loss of both machines is almost the same, but the AF-FePM can suppress the increase in motor loss even at low switching frequencies. As a result, the total system loss of the AF-FePM can be lower than that of the RF-NdPM at $f_{sw} = 5$ kHz.

VII. Conclusion

In this paper, we evaluated the effect that the PWM harmonic current has on the proposed AF-FePM and on a commercially available RF-NdPM mounted in a Honda Freed. The following conclusions were reached for each investigation and evaluation.

1) As a preliminary step toward the analytical comparison, PWM harmonic currents were evaluated in experiments using a prototype AF-FePM to confirm the accuracy of the PWM harmonic current used in FEA. As a result, the THD of the calculated and measured currents were 4.79% and 4.87%, respectively, which showed good agreement. Additionally, FEA-predicted efficiency of the AF-FePM considering the harmonic current and the measured efficiency were almost matched at representative operating points. Accordingly, we concluded that the efficiency of actual machines can be predicted with relatively high accuracy by considering PWM harmonic currents in FEA.
2) The THD of the harmonic current in the AF-FePM was higher than that of the RF-NdPM in all operating region because of the greater number of poles. However, the AF-FePM can moderate the increase in harmonic loss despite having a higher THD of input current. This is because the iron loss density of the SMC used for the AF-FePM in the high-frequency region is lower than the LSS for the RF-NdPM. Furthermore, it was found that the round copper wire and ferrite PM also contributed to suppressing the increase in PWM harmonic losses in the AF-FePM. On the other hand, it should be noted that applying other materials to the AFPM may eliminate these benefits against the PWM harmonic loss.
3) Loss of both machines was compared for a WLTC driving cycle. In the analysis with the sinusoidal current, the total energy loss in the WLTC driving cycle was almost identical for the two systems, but when the PWM harmonics were taken into consideration the AF-FePM was able to suppress any increase in the total loss, resulting in a total loss reduction of 15.9% compared to the RF-NdPM. Accordingly, we saw that the AF-FePM has superior efficiency than the RF-NdPM for the PWM harmonic current, which comes from the PWM inverter.
4) The total system loss considering the inverter loss when changing the switching frequency was evaluated at representative operating points. As a result, this paper revealed that the total system loss can be reduced by setting the switching frequency to 5 kHz in both machines. Eventually, the total system loss of the proposed AF-FePM was lower than that of the RF-NdPM.

Based on the above conclusions, the proposed AF-FePM can be realized at low cost, has high motor efficiency, and can improve system efficiency including the inverter. Therefore, it can be considered.

References

[1] O. H. Hannisdahl, H. V. Malvik, and G. B. Wensaas, "The future is electric! The EV revolution in Norway-explanations and lessons learned," in *Proc. IEEE 2013 World Electric Veh. Symp. Exhib.*, 2013, pp. 1–13.
[2] EV Volumes, EV Data Center, 2023. [Online]. Available: https://www.ev-volumes.com
[3] K. Izumiya, R. Tsunata, M. Takemoto, J. Imai, T. Saito, and T. Ueno, "Axial-flux machine using ferrite PM and round wire competitive to radial-flux machine using Nd-Fe-B PM for HEV traction," in *Proc. IEEE Int. Conf. Elect. Machines*, 2022, pp. 192–198.

[4] P. Fyhr, G. Domingues, A. Reinap, M. Andersson, and M. Alaküla, "Performance and manufacturability tradeoffs of different electrical machine designs," in *Proc. IEEE Int. Electric Machines Drives Conf.*, 2017, pp. 1–7.
[5] S. Soma, S. Fujishiro, and E. Shirado, "Research of the heavy-rare-earth-free motor for hybrid vehicle," *Trans. Soc. Automot. Engineers Jpn.*, vol. 48, no. 5, pp. 1079–1083, Sep. 2017.
[6] T. -C. Jeong et al., "Current harmonics loss analysis of 150-kW traction interior permanent magnet synchronous motor through Co-analysis of d-q axis Current control and finite element method," *IEEE Trans. Magn.*, vol. 49, no. 5, pp. 2343–2346, May 2013.
[7] A. Krings, J. Soulard, and O. Wallmark, "PWM influence on the iron losses and characteristics of a slotless permanent-magnet motor with SiFe and NiFe stator cores," *IEEE Trans. Ind. Appl.*, vol. 51, no. 2, pp. 1475–1484, Mar./Apr. 2015.
[8] Y. Miyama, M. Hazeyama, S. Hanioka, N. Watanabe, A. Daikoku, and M. Inoue, "PWM carrier harmonic iron loss reduction technique of permanent-magnet motors for electric vehicles," *IEEE Trans. Ind. Appl.*, vol. 52, no. 4, pp. 2865–2871, Jul./Aug. 2016.
[9] B. Wex, S. Silber, K. Kaspar, and W. Gruber, "Fully automatized PWM loss calculation in multiphase PMSM and experimental verification," *IEEE Trans. Ind. Appl.*, vol. 58, no. 4, pp. 4237–4247, Jul./Aug. 2022.
[10] P. Sergeant, H. Vansompel, A. Hemeida, A. V. d. Bossche, and L. Dupré, "A computationally efficient method to determine iron and magnet losses in VSI-PWM fed axial flux permanent magnet synchronous machines," *IEEE Trans. Magn.*, vol. 50, no. 8, Aug. 2014, Art. no. 8101710.
[11] T. Xiao, J. Li, K. Yang, J. Lai, and Y. Lu, "Study on AC copper losses in an air-cored axial flux permanent magnet electrical machine with flat wires," *IEEE Trans. Ind. Electron.*, vol. 69, no. 12, pp. 13255–13264, Dec. 2022.
[12] R. Tsunata, M. Takemoto, J. Imai, T. Saito, and T. Ueno, "The superiority of efficiency considering harmonic current caused by PWM inverter in Axial-flux PM machine using Ferrite PM for traction applications: Comparison to Radial-Flux PM machines using NdFeB PM," in *Proc. IEEE Energy Convers. Congr. Expo.*, 2023, pp. 3745–3752.
[13] Y. Gao, R. Qu, D. Li, J. Li, and L. Wu, "Design of three-phase flux-reversal machines with fractional-slot windings," *IEEE Trans. Ind. Appl.*, vol. 52, no. 4, pp. 2856–2864, Jul./Aug. 2016.
[14] R. Tsunata, M. Takemoto, S. Ogasawara, A. Watanabe, T. Ueno, and K. Yamada, "Development and evaluation of an axial gap motor using neodymium bonded magnet," *IEEE Trans. Ind. Appl.*, vol. 54, no. 1, pp. 254–262, Jan./Feb. 2018.
[15] R. Tsunata, M. Takemoto, S. Ogasawara, T. Saito, and T. Ueno, "SMC development guidelines for axial flux PM machines employing coreless rotor structure for enhancing efficiency based on experimental results," *IEEE Trans. Ind. Appl.*, vol. 58, no. 3, pp. 3470–3485, May–Jun. 2022.
[16] D. Azuma, Y. Enokizono, T. Saito, T. Ishimine, and T. Ueno, "Investigation of the influence of harmonics on iron loss of soft magnetic composites," in *Proc. IEEE Int. Conf. Elect. Machines*, 2022, pp. 1124–1129.
[17] C. M. Apostoaia, "AC machines and drives simulation platform," in *Proc. IEEE Int. Electric Machines Drives Conf.*, 2013, pp. 1295–1299.
[18] I. Talebian and N. Rostami, "Co-simulation of a surface-mounted permanent magnet synchronous motor drive using finite element method," in *Proc. IEEE Int. Power Renewable Energy Conf.*, 2021, pp. 1–6.
[19] A. Ahagon, K. Matsunaga, H. Ebrahimi, K. Semba, T. Yamada, and K. Narita, "Investigation on behavior model of PMSMs considering AC copper losses with Cauer circuit," in *Proc. IEEE 20th Biennial Conf. Electromagn. Field Computation*, 2022, pp. 1–2.
[20] R. Tsunata, M. Takemoto, J. Imai, T. Saito, and T. Ueno, "A proposal of an axial-flux permanent-magnet machine employing SMC core with tooth-tips constructed by one-pressing process: Improving torque and manufacturability," *IEEE Access*, vol. 11, pp. 109435–109447, 2023, doi: 10.1109/ACCESS.2023.3321829.
[21] F. Giulii Capponi, G. De Donato, and F. Caricchi, "Recent advances in axial-flux permanent-magnet machine technology," *IEEE Trans. Ind. Appl.*, vol. 48, no. 6, pp. 2190–2205, Nov./Dec. 2012.
[22] L. Wang, Z. Q. Zhu, H. Bin, and L. M. Gong, "Current harmonics suppression strategy for PMSM with nonsinusoidal back-EMF based on adaptive linear neuron method," *IEEE Trans. Ind. Electron.*, vol. 67, no. 11, pp. 9164–9173, Nov. 2020.
[23] Z. Tang and B. Akin, "A new LMS algorithm based deadtime compensation method for PMSM FOC drives," *IEEE Trans. Ind. Appl.*, vol. 54, no. 6, pp. 6472–6484, Nov./Dec. 2018.
[24] S. Steentjes, S. Boehmer, and K. Hameyer, "Permanent magnet eddy-current losses in 2-D FEM simulations of electrical machines," *IEEE Trans. Magn.*, vol. 51, no. 3, Mar. 2015, Art. no. 6300404.
[25] S. Y. Oh et al., "Design of IPMSM rotor shape for magnet eddy-current loss reduction," *IEEE Trans. Magn.*, vol. 50, no. 2, pp. 841–844, Feb. 2014.
[26] R. Sahu, P. Pellerey, and K. Laskaris, "Eddy current loss model unifying the effects of reaction field and non-homogeneous 3-D magnetic field," *IEEE Trans. Magn.*, vol. 56, no. 2, Feb. 2020, Art.no. 7508404.
[27] J. Ma and Z. Q. Zhu, "Magnet Eddy current loss reduction in permanent Magnet machines," *IEEE Trans. Ind. Appl.*, vol. 55, no. 2, pp. 1309–1320, Mar./Apr. 2019.
[28] S. Zhu, M. Cheng, and Y. Zhu, "Fast calculation of PM Eddy current loss in IPMSM under PWM VSI supply based on the spectra of line-line voltage," *IEEE Trans. Magn.*, vol. 54, no. 11, Nov. 2018, Art. no. 6300405.
[29] H. -W. Lee, S. -J. Jang, and K. -B. Lee, "Advanced DPWM method for switching loss reduction in isolated DC type dual inverter with open-end winding IPMSM," *IEEE Access*, vol. 11, pp. 2700–2710, 2023.
[30] T. -C. Jeong et al., "Current harmonics loss analysis of 150-kW traction interior permanent magnet synchronous motor through Co-analysis of d-q axis Current control and finite element method," *IEEE Trans. Magn.*, vol. 49, no. 5, pp. 2343–2346, May 2013.
[31] R. Tsunata, K. Izumiya, M. Takemoto, J. Imai, T. Saito, and T. Ueno, "Designing and prototyping an axial-flux machine using ferrite PM and round wire for traction applications: Comparison with a radial-flux machine using Nd-Fe-B PM and rectangular wire," *IEEE Trans. Ind. Appl.*, vol. 60, no. 3, pp. 3934–3949, May–Jun. 2024, doi: 10.1109/TIA.2024.3371959.
[32] M. Ben-Marzouk, S. Pelissier, G. Clerc, A. Sari, and P. Venet, "Generation of a real-life battery usage pattern for electrical vehicle application and aging comparison with the WLTC profile," *IEEE Trans. Veh. Technol.*, vol. 70, no. 6, pp. 5618–5627, Jun. 2021.
[33] R. Tsunata, M. Takemoto, J. Imai, T. Saito, and T. Ueno, "Comparison of thermal characteristics in various aspect ratios for radial-flux and axial-flux permanent magnet machines," *IEEE Trans. Ind. Appl.*, vol. 59, no. 3, pp. 3353–3367, May–Jun. 2023.
[34] A. Hoevenaars, M. McGraw, and C. Burley, "A practical application of a sinewave filter to resolve ESP motor failures," in *Proc. IEEE Petroleum Chem. Ind. Committee Conf.*, 2019, pp. 311–320.
[35] M. Buffolo et al., "Review and outlook on GaN and SiC power devices: Industrial State-of-the-art, applications, and perspectives," *IEEE Trans. Electron Devices*, vol. 71, no. 3, pp. 1344–1355, Mar. 2024.
[36] S. Hori et al., "Application of variable carrier frequency control by using wide bandgap semiconductors inverter for WLTC mode driving," in *Proc. IEEE 22nd Int. Conf. Ind. Technol.*, 2021, pp. 322–326.
[37] B. Zheng, J. Zou, Y. Xu, G. Yu, L. Wang, and P. Zanchetta, "High-frequency current harmonic analysis and suppression in dual three-phase PMSMs with advanced carrier phase-shift PWM," *IEEE Trans. Power Electron.*, vol. 39, no. 2, pp. 2569–2581, Feb. 2024.
[38] D. Ye et al., "Variable switching sequence PWM strategy of dual three-phase machine drive for high-frequency current harmonic suppression," *IEEE Trans. Power Electron.*, vol. 35, no. 5, pp. 4984–4995, May 2020.
[39] F. Casanellas, "Losses in PWM inverters using IGBTs," *IEE Proc. - Electric Power Appl.*, vol. 141, no. 5, pp. 235–239, 1994.
[40] J. W. Kolar, H. Ertl, and F. C. Zach, "How to include the dependency of the RDS(on) of power MOSFETs on the instantaneous value of the drain current into the calculation of the conduction losses of high-frequency three-phase PWM inverters," *IEEE Trans. Ind. Electron.*, no. 3, vol. 45, pp. 369–375, Jun. 1998.

Ren Tsunata was born in Miyagi Prefecture, Japan, in 1992. He received the B.S., M.S., and Ph.D. degrees in electrical engineering from Hokkaido University, Hokkaido, Japan, in 2015, 2017, and 2021, respectively. From 2017 to 2018, he was with Toyota Motor Corporation, Aichi, Japan. In 2021, he joined Okayama University as a Research Fellow. He became an Assistant Professor with the Graduate School of Natural Science and Technology, Okayama University, Okayama, Japan, in 2022, and has been a Research Associate Professor since 2023. His research interests include permanent magnet synchronous machines, variable flux motors, and axial flux machines. Dr. Tsunata is a member of the Institute of Electrical Engineers of Japan and The Japan Society of Applied Electromagnetics and Machines. Dr. Tsunata was the recipient of four IEEJ Excellent Presentation Awards in 2017, 2020, 2022, and 2023, and Incentive Award from JSAEM in 2020.

Masatsugu Takemoto was born in Tokyo, Japan, in 1972. He received the B.S. and M.S. degrees in electrical engineering from the Tokyo University of Science, Noda, Japan, in 1997 and 1999, respectively, and the Ph.D. degree in electrical engineering from the Tokyo Institute of Technology, Tokyo, Japan, in 2005. In 1999, he joined the Department of Electrical Engineering, Tokyo Institute of Technology as a Research Associate. In 2004, he joined the Department of Mechanical Systems Engineering, Musashi Institute of Technology, Tokyo, as a Research Associate, where he became a Lecturer in 2005. In 2008, he joined Hokkaido University as an Associate Professor with the Graduate School of Information Science and Technology. Since 2020, he has been with Okayama University, where he is currently a Professor with the Graduate School of Natural Science and Technology. He is engaged in research on permanent magnet synchronous motors, axial gap motors, rare-earth-free motors, bearingless motors, and magnetic bearings. Dr. Takemoto is a member of IEEJ. He was the recipient of the Nagamori Award from the Nagamori Foundation in 2017, IEEJ Transaction Paper Award in 2005, Prize Paper Awards from the Electric Machines Committee of the IEEE Industry Applications Society in 2011 and 2019, and Prize Paper Award from the Electrical Machines Technical Committee of the IEEE Industrial Electronics Society in 2018. He was a Secretary, the Vice-Chair, and Chair of the IEEE IAS Japan chapter during 2008–2009, 2010–2011, and 2012–2013, respectively.

Jun Imai was born in Okayama Prefecture, Japan, in 1964. He received the B.S., M.S., and Ph.D. degrees in electrical engineering from the Department of Electrical Engineering, Kyushu University, Fukuoka, Japan, in 1987, 1989, and 1992, respectively. He became a Lecturer with Okayama University in 2000 and has been an Associate Professor since 2008. His main research interests include the modeling and control of distributed parameter systems, especially in performance limitation issues of physical control systems.

Tatsuya Saito was born in Kyoto, Japan, in 1987. He received the B.S., M.S., and Ph.D. degrees in material science from Tohoku University, Sendai, Japan, in 2009, 2011, and 2014, respectively. Since 2014, he has been with Sumitomo Electric Industries, Ltd., Hyogo, Japan, where he is engaged in research on soft magnetic materials and powder metallurgy.

Tomoyuki Ueno was born in Wakayama Prefecture, Japan, in 1976. He received the B.S. and M.S. degrees in mechanical engineering from Kobe University, Hyogo, Japan, in 1999 and 2001, respectively, and the Dr. Eng. degree in industrial innovation science from Okayama University, Okayama, Japan, in 2015. Since 2001, he has been with Sumitomo Electric Industries, Ltd., where he is engaged in research on soft magnetic materials, ceramic materials, and cutting and grinding technology. Dr. Ueno is a member of the Japan Society and Power Metallurgy and the Japan Society for Abrasive Technology. He was the recipient of the JSPM Award Innovatory Research in 2009, JSAT Prize Paper Award in 2012, Prize Paper Award from the Machine Tool Engineer Foundation in 2012, and JSPM Award for Innovatory Development in 2013.